Full Length Article

Iron carbide encapsulated by porous carbon nitride as bifunctional electrocatalysts for oxygen reduction and evolution reactions

Liangqin Wei, Hongdi Sun, Tiantian Yang, Shenzhen Deng, Mingbo Wu, Zhongtao Li *

State Key Laboratory of Heavy Oil Processing, College of Chemical Engineering, China University of Petroleum (East China), Qingdao 266580, People's Republic of China

A R T I C L E I N F O

A B S T R A C T

Herein, the study reports a facile and scale-up able strategy to synthesize metal organic frameworks (MOFs) Fe-7,7,8,8-Tetracyanoquinodimethane (Fe-TCNQ) as precursors to develop non-precious metal bifunctional electrocatalysts through a one-step hydrothermal route. Then, Fe_3C/carbon nitride ($Fe_3C@CN_x$) core-shell structure composites are readily available through pyrolyzing Fe-TCNQ at reasonable temperature, during which hierarchical porous structures with multimodal porosity formed. Nitrogen doped porosity carbon layers can facilitate mass access to active sites and accelerate reaction. Consequently, the optimized catalyst exhibits superior oxygen reduction reaction (ORR) electrocatalytic activity and better catalytic activity for oxygen evolution reaction (OER) in alkaline medium than that of Pt/C, which can be attributed to the synergistic effect of strong coupling between Fe_3C and nitrogen doped carbon shells, active sites Fe-N_X, optimal level of nitrogen doping, and appropriate multimodal porosity.

© 2018 Published by Elsevier B.V.

1. Introduction

Owning to increase of energy consumption and environmental degradation, the energy conversion and storage devices with high energy density, environmental benignity and low cost have gained increasing attentions [1–3]. Among these energy devices, fuel cell and metal−air batteries are considered as most competent candidates because of their high energy density, possessing great prospective in commanding electric vehicles (EVs) with long-range competence and flexible electronic devices. However, the sluggish oxygen reduction reaction (ORR) during the discharge process and oxygen evolution reaction (OER) during the charge process are impediment the widespread of regenerative fuel cells and rechargeable metal−air batteries, which intensively depend upon exploration of active and durable novel electrocatalysts. Currently, noble metals platinum is classical ORR catalyst for the desired four-electron transfer ORR process but poor for OER [4,5]. Meanwhile, high cost, scarcity, vulnerable to methanol poisoning, and instability of noble metal hamper it's wide application in the fuel cells and metal-air battery [6].

Recently, tremendous efforts have been devoted to exploring nonprecious metal catalysts substitute for noble metal. Including transition metal oxides [7], metallic sulphide [8], metal-N_4 macro-

cycles [9] and some transition metal cations [10]. Among them, Fe-N-C catalysts have been intensively studied due to their superior catalytic performance and stability as electrode material in place of commercial Pt/C [11], some of which possess core-shell structure with Fe/Fe_3C encapsulated in nitrogen doped carbon that exhibit highly catalytic activity [12,13]. Li et al. synthesized Fe_3C nanoparticles encapsulated in graphitic shells as ORR catalysts, interestingly, the catalyst activity of ORR showed obvious recession after removing the Fe_3C nanoparticles [12]. Besides, Li's research demonstrates that Fe/Fe_3C also has excellent OER catalytic activity [14]. It is believed that the encased Fe/Fe_3C core could active the outside surface of the graphitic shells due to a unique host–guest electronic interaction changes the local work function of the carbon layers, which facilitates improve the catalytic activity [15].

So far, Fe-N-C catalysts that derived from metal–organic frameworks (MOFs) have attracted some attentions due to diverse composition, ultrahigh surface area, ordered and controllable porous structure. The well dispersion of metal atoms in MOFs and easily modification of ligands render MOFs as idea procures to develop advanced electrocatalysts, which could maintain porosity and more catalytic active site after pyrolysis. For example, iron carbide nanoparticles-embedded carbon nanotubes derived from Fe-based MIL-88B nanorods that embedded in Zn-based ZIF-8 polyhedron have been developed as the high performance ORR catalysts. On account of thin graphitic carbon layer and porous structure

facilitate the charge and mass transport within Fe₃C particles, carbon matrix might grant high robustness and provide extra protection to Fe₃C crystallites [16]. Lan's group reported that Fe/Fe₃C@graphitic layer/carbon nanotube hybrid derived from MIL-101 (Fe) exhibited good bifunctional electrocatalytic activity for ORR and OER [17]. However, some synthetic methods of catalysts in previous reports are somewhat complicated or catalytic performance of some catalysts are not desirable.

Herein, a facile and scale-up able strategy to synthesize a MOFs Fe-7,7,8,8-Tetracyanoquinodimethane (Fe-TCNQ) as precursors has been developed through a one-step hydrothermal route. Then, well-defined Fe₃C nanoparticles that encapsulated in graphitic carbon nitride shells formed after pyrolysis. Not only the method could achieved high yield by a simple synthetic method, but also lead to the stable and uniform product. Not only the method could achieved high yield by a simple synthetic method, but also lead to the stable and uniform product [15]. As illustrated in Scheme 1, a hierarchical porous structure with multimodal porosity formed during pyrolysis process, in which abundant mesoporosity can facilitate access to active sites and enhance mass transport. Consequently, the optimized catalyst exhibited superior ORR electrocatalytic activity comparable to Pt/C in an alkaline medium and it showed good catalytic activity for OER as well, which can be attributed to the synergistic effect strong coupling between Fe₃C and nitrogen doped carbon shells [15], optimal level of nitrogen doping and appropriate multimodal porosity.

2. Experimental section

2.1. Synthesis of Fe-TCNQ -800, Fe-TCNQ-900, Fe-TCNQ-1000

The precursors were synthesized through one-pot hydrothermal method. During a synthesis process, 20 mmol 7,7,8,8-Tetracyanoquinodimethane (TCNQ) and 20 mmol iron acetate were dissolved in 60 mL N, N-dimethylformamide (DMF) and sonicated for 1 h to form a homogenous suspension. Then, the suspension was quickly transferred into 80 mL Teflon-lined stainless-steel autoclave and maintained at 150 °C for 10 h. The dark green precursor was collected by centrifuging, washing and drying at 60 °C overnight. About 3 g of Fe-TCNQ precursor was readily obtained through one-step synthesis. Subsequently, the precursor was heated to a pyrolysis temperature in the range of 800–1000 °C with 5 °C min⁻¹ and maintained at the pyrolysis temperatures for 2 h under a flow of N₂. The catalysts were defined as Fe-TCNQ-800, Fe-TCNQ-900, and Fe-TCNQ-1000 based on the pyrolysis temperature, respectively.

2.2. Synthesis of TCNQ-900 and Fe-TCNQ-mix-900

For comparison, the TCNQ-900 sample was prepared under the same conditions for synthesizing Fe-TCNQ-900 without addition of iron acetate. Procures of Fe-TCNQ-mix-900 was made by merely mixing TCNQ and iron acetate through grinding in a mortar. More-over, pyrolysis processes are executive same as that of Fe-TCNQ-900.

2.3. Characterization

The morphology and nanostructure of catalysts were characterized by Transmission electron microscopy (TEM, JEM-2010UHR, Japan) and high-resolution transmission electron microscopy (HRTEM). The crystal outline and structure of the catalysts were characterized by X-ray diffraction (XRD, Bruker D8-Advance diffractometer with Cu Kα). The elemental valences of the samples were conducted using X-ray photoelectron spectroscopy (XPS, Thermo Scientific ESCALab250Xi). The Raman spectra were carried out on a Renishaw DXR Raman spectroscopy system. Specific surface areas were investigated by Brunauer-Emmett-Teller (BET) nitrogen adsorption-desorption (Micromeritics, ASAP 2050, America).

2.4. Electrochemical measurements

Electrochemical measurements were performed with a 760E Bipotentiostat (CH Instruments) and rotator (RDE Research Instrumentation) at room temperature using a three-electrode electrochemical cell. A Pt column and Ag/AgCl were used as the counter and reference electrode, respectively. The working electrode was a rotating disk electrode with a glassy carbon disk (GCE, 4 mm in diameter). The catalyst ink was prepared by adding 2 mg of powder into a solution containing 800 μL ethanol and 5 μL Nafion (5%) to form a homogeneous suspension at the catalyst concentration of 2.5 mg ml⁻¹. 10 μL of the inks was pipetted onto the clean GCE surface (mass loading is 200 ug cm⁻²).

ORR measurement: Linear sweep voltammograms (LSV) were acquired in an O₂-saturated 0.1 M KOH aqueous solution at various rotation rates (400–2500 rpm). Cyclic voltammograms (CV) were acquired at range of −1 V to 0.2 V (vs. Ag/AgCl) with scan rate of 50 mV s⁻¹. The transfer electron number (n) was calculated by the Koutechy–Levich (K–L) equation:

$$J^{-1} = J_L^{-1} + J_K^{-1} = (B\omega^{1/2})^{-1} + J_K^{-1} \tag{1}$$

$$B = 0.62nFC_0(D_0)^{2/3}\nu^{-1/6} \tag{2}$$

where J, J_K and J_L are the measured current density, the kinetic and diffusion limiting current densities, respectively, ω is the rotation rate, ν is the kinetic viscosity of the electrolyte (0.01 cm² s⁻¹ for 0.1 M KOH solution), F is the Faraday constant (F = 96,485 C mol⁻¹), C₀ is the concentration of O₂ (1.2 × 10⁻³ mol L⁻¹ for 0.1 M KOH solution), D₀ is the diffusion coefficient of O₂ (1.93 × 10⁻⁵ cm² s⁻¹ for 0.1 M KOH solution).

OER measurement: With the same scan rate to ORR LSV measurements, but were acquired in an N₂-saturated 0.1 M KOH aqueous solution. and the OER LSV measurements were conducted at the potential from 0.2 to 1.1 V (vs. Ag/AgCl).
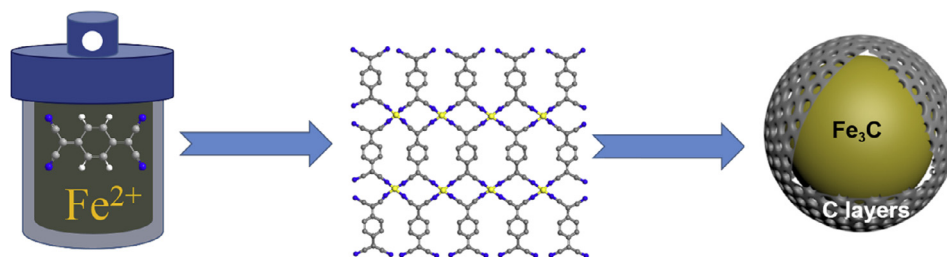
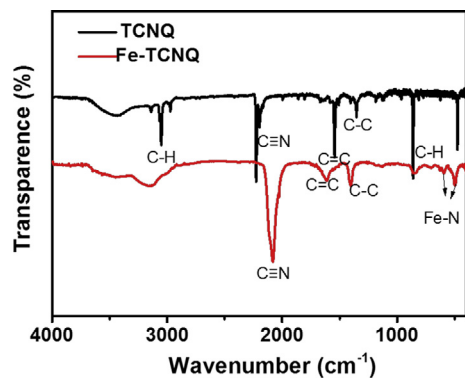**Scheme 1.** Illustration of the preparation process of the Fe₃C@CNx.

Fig. 1. FT-IR spectra for TCNQ molecule and Fe-TCNQ.

3. Results and discussion

Fourier transform infrared (FT-IR) spectra were firstly carried out to verify the formation of Fe-7,7,8,8-Tetracyanoquinodimethane (Fe-TCNQ) during solvothermal process (Fig. 1). The FT-IR spectrum of 7,7,8,8-Tetracyanoquinodimethane (TCNQ) displays the peaks at 2225 cm^{-1}, 1542 cm^{-1}, 1353 cm^{-1}, and 861 cm^{-1} characteristics of C≡N, C=C, C—C stretching vibration and C—H bending vibration adsorption peaks [18]. While C≡N stretching vibration at 2081 cm^{-1} in the Fe-TCNQ generates bathochromic shift compared with that of TCNQ (2225 cm^{-1}). Which was mainly due to the Iron coordinated with cyanide during the solvothermal procedure. And stretching vibration band of C=C (1611 cm^{-1}) and C—C (1401 cm^{-1}) generates blue shift, that may be attributed to TCNQ as a receptor to get electrons from Fe^{2+} after forming metal

coordination compounds [18]. Importantly, the newly peaks emerged at 594 cm^{-1} and 496 cm^{-1} suggest the formation of Fe-N [19], which represented the formation of MOFs.

The crystalline structure was also examined by XRD. As shown in Fig. S1a, Fe-TCNQ exhibited clear and sharp diffraction peaks, which indicated good crystallinity. While, the XRD data of some other metal-TCNQ compounds also shown strong and sharp diffraction peaks, which could be ascribe to the formation of well-ordered MOF structure [20]. And the nanostructures of Fe-TCNQ was characterized by TEM (Fig. 2a) and SEM (Fig. S1b), precursors lamellar Fe-TCNQ subunits cross-linked with each other to form porous network structures [20]. After pyrolysis, Fe-TCNQ -900 was consisted with spherical core-shell nanoparticle with 5 nm thick shell and 20–60 nm diameter in total. The detailed characteristics of Fe-TCNQ-900 were displayed in Fig. 2b and c, which showed that most Fe$_3$C nanoparticles were encapsulated by graphitic layers. HRTEM image in Fig. 2c revealed that the core section was also crystallized with a lattice distance of 0.200 nm, which was consistent with planes of (0 3 1) in the Fe$_3$C phase. During heat treatment, Fe was formed by the decompose of coordinate bonds in Fe-TCNQ, which could catalyze the growth of carbon coating at higher temperature. Meanwhile, parts of carbon dissolved in Fe formed Fe$_3$C crystalline in core section. And the morphology of Fe-TCNQ-800, Fe-TCNQ -1000, and Fe-TCNQ-mix-900 were also observed by TEM (Fig. S2), Fe-TCNQ-800 was mainly composed of spherical nanoparticles with a diameter from 20–50 nm. As the pyrolysis temperature increased, the diameter of Fe-TCNQ-900 nanoparticles increased to 100–200 nm due to aggregations of iron. While in Fe-TCNQ-mix-900, the diameter of nanoparticles increased to 300–400 nm due to the poor dispersion of Fe in precursor. XRD patterns of the as-prepared Fe-TCNQ-800, -900, -1000 are shown in Fig. 2d. The diffraction peak at 44.7° and 65°
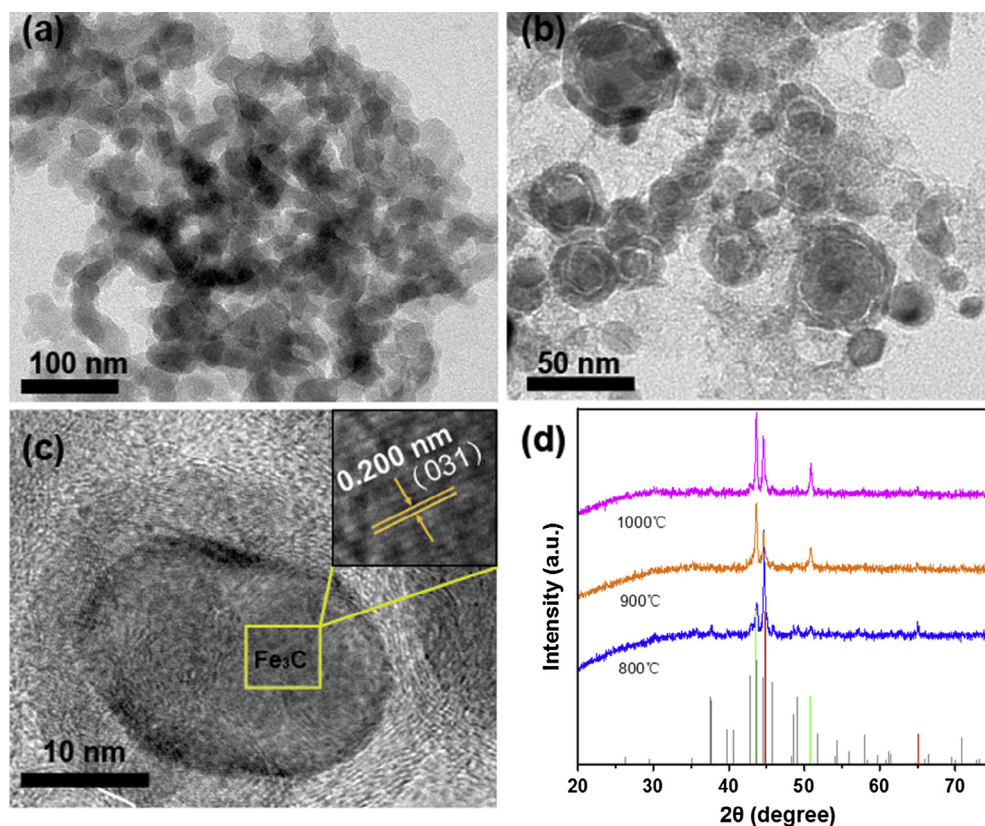

Fig. 2. (a) TEM image of Fe-TCNQ precursors. (b) TEM image ofFe-TCNQ-900 catalyst. (c) HRTEM image of Fe$_3$C@C nanosphere in Fe-TCNQ-900 catalyst, inset is the HRTEM image showing the lattice fringes of Fe$_3$C core. (d) XRD patterns ofFe-TCNQ-800, -900, -1000.
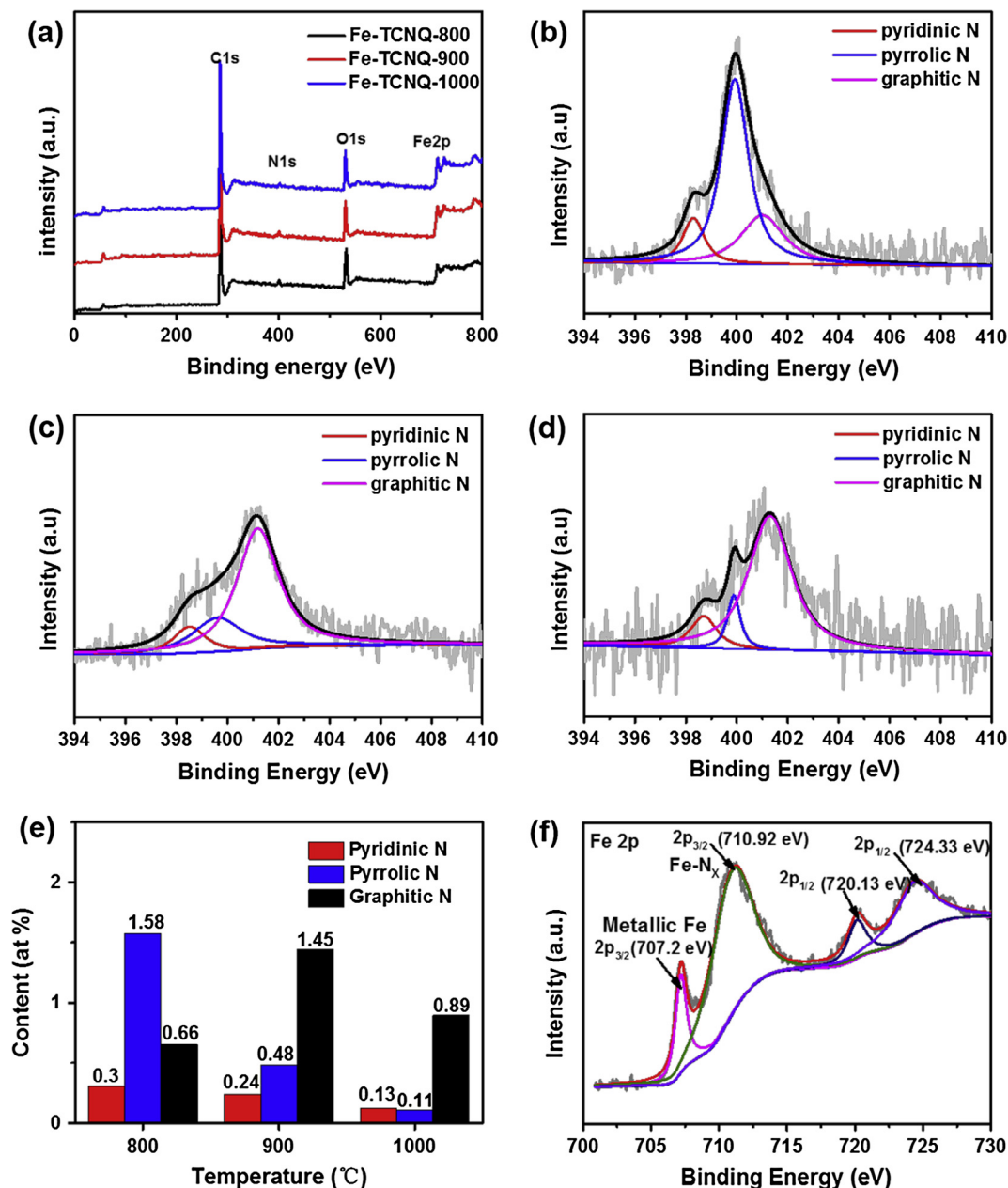
Fig. 3. (a) XPS survey of Fe-TCNQ-800, -900, -1000, respectively. High-resolution N 1s XPS spectra of (b) Fe-TCNQ-800. (c) Fe-TCNQ-900. (d) Fe-TCNQ-1000. (e) The content of pyridinic N, pyrrolic N, and graphitic N of Fe-TCNQ-800, -900, -1000, respectively. (f) High-resolution Fe 2p of Fe-TCNQ-900.

were indexed to (110) and (200) planes of Fe (JCPDS, No. 06-0696), and a certain amount of $FeN_{0.0324}$ (JCPDS, No. 75-2127) related to 43.6° and 51.8° were found in the three samples. Besides, the rest peaks were consistent with the crystalline planes of Fe_3C (JCPDS, No. 35-0772). Compared with Fe-TCNQ-800, the contents of Fe crystal in Fe-TCNQ-900 and Fe-TCNQ-1000 were decreased and the diffraction peak of Fe_3C increased, which suggested that part of Fe was reacted with carbon and transformed into Fe_3C crystalline at higher temperature.

To identify the chemical bonding configurations on the surface of nanohybrids, XPS spectrums ofFe-TCNQ-800, Fe-TCNQ-900, and Fe-TCNQ-1000 were tested. In Fig. 3a, the C, N, O and Fe signals could be detected in all the catalysts. The concentrations of all the elements in the three samples were shown in the Table 1, which showed that concentrations of Fe element in the Fe-TCNQ -900 is the highest among all the samples, High levels of iron

was inclined to form more active catalytic species like Fe_3C and Fe-N_X to enhance electrocatalytic performance. The high-resolution N1s spectrum of the Fe-TCNQ-800, Fe-TCNQ-900, and Fe-TCNQ-1000 could be deconvoluted into three peaks corresponding to pyridinic N (398.5 eV), pyrrolic N (399.7 eV) and graphitic N (401.1 eV), respectively(Fig. 3b–d) [21,22], which supports the successful doping of N into the carbon matrix [23–25]. Previous report have proved that pyridinic and pyrrolic N could be coordinated with Fe to form Fe-N_X bonds [26,27]. And pyridinic and graphitic N are considered as efficient active sites for ORR [26,28]. Furthermore, according to the integral area of corresponding peaks, the concentrations of the different types of nitrogen were shown in Fig. 3e and Table S1. The content of total N dropped off and pyridinic N and pyrrolic N were also gradually decreased to zero with the temperatures increasing. While, the concentration of graphitic N in Fe-TCNQ-900 (1.45 at.%) was the

Catalysts	C (at.%)	O (at.%)	N (at.%)	Fe (at.%)
Fe-TCNQ-800	82.48	13.13	2.54	1.85
Fe-TCNQ-900	82.36	11.12	2.17	4.35
Fe-TCNQ-1000	84.85	10.25	1.13	3.77

highest among all samples, which revealed higher thermostability than other types N [29]. The doping of graphitic N into carbon matrix leads to non-uniform electron distribution and make the C—N bonds much shorter, which significantly enhance catalytic activity of carbon [30,31]. Furthermore, The high-resolution scan of Fe 2p electrons of Fe-TCNQ-900 was shown in the Fig. 3f, By deconvolution, the high resolution Fe $2p_{3/2}$ could be assigned to metallic Fe (707.2 eV) and Fe-N_X (710.92 eV) [32,33].

The degree of graphitization of carbon was analyzed by Raman measurements where the graphitic D and G bands were located at 1350 and 1593 cm^{-1}, respectively (Fig. 4a); [34,35]. The integral intensity ratio of I_D/I_G of the samples varied slightly under different pyrolysis temperature (0.97 of Fe-TCNQ-800, 0.93 of Fe-TCNQ-900, 0.92 of Fe-TCNQ-1000). More graphitic carbon with fewer defects would be formed at higher temperature, which would improve the conductivity and thus promote charge transfer. When the carbonization temperatures rose over 900 °C, the I_D/I_G ratio were similar, which would be due to the aggregation of Fe$_3$C slow down the growth of graphitic layer on surface. The BET specific surface area and pore size distributions were investigated by N$_2$ adsorption/desorption measurements (Fig. 4b, c). BET surface areas were 157 m^2 g^{-1} of Fe-TCNQ-800, 114 m^2 g^{-1} of Fe-TCNQ-900 and 104 m^2 g^{-1} of Fe-TCNQ-1000, respectively. The specific surface area decreased with the pyrolysis temperature increasing, probably because of partial shrinkage of the carbon skeleton at higher

temperatures. Utilizing the BJH model, the pore size distribution derived from the corresponding adsorption isotherm revealed pore diameters of all samples range from 2 to 100 nm, indicating that the mesoporous and macroporous structures. It is believed that the mesopores and macropores facilitate the mass transfer of the related species such as O$_2$, H$_2$O and OH$^-$, thus enhancing the electrocatalytic activity [34,36].

The ORR electrocatalytic activities of Fe-TCNQ-900 were evaluated by CV in N$_2$ and O$_2$ saturated 0.1 M KOH (Fig. 5a). Compare with N$_2$-saturated electrolyte, a well-defined oxygen reduction peak located at −0.16 V in O$_2$. To further investigated the effect of pyrolysis temperature on catalytic activity, LSV curves were obtained. As displayed in the Fig. 5b, Fe-TCNQ-900 exhibited best ORR activity with onset potential −0.029 V, which was comparable to commercial Pt/C. Moreover, the diffusion-limiting current was slightly higher than that of Pt/C, which can be ascribe to core-shell structure of Fe$_3$C@CNx, optimal degree of graphitization and appropriate number of nitrogen active sites. Both onset potential and half-wave potential of Fe-TCNQ-800 were more negative than those of Fe-TCNQ-900 and Fe-TCNQ-1000, due to the lower content of graphitic nitrogen and graphitization degree [37], which indicated that the graphitic carbon structure can not only better protect the Fe$_3$C cores, but also enhance charge and mass transfer during ORR. When the pyrolysis temperature rose up to 1000 °C, catalytic activity also decreased owing to low content of N and aggregation of ferric nanoparticles.

Furthermore, to study the influence of uniformly dispersed Fe atom in MOFs on final catalytic activity, two control samples were synthesized and evaluated by LSV measurement (Fig. 5c). As one control sample, TCNQ-900 (without addition of iron acetate) exhibited the worst ORR activity (most negative E$_{1/2}$ and lowest limiting diffusion current), which would be due to the absent of more active Fe-Nx and Fe$_3$C [38]. Another control catalyst Fe-TCNQ-mix-900
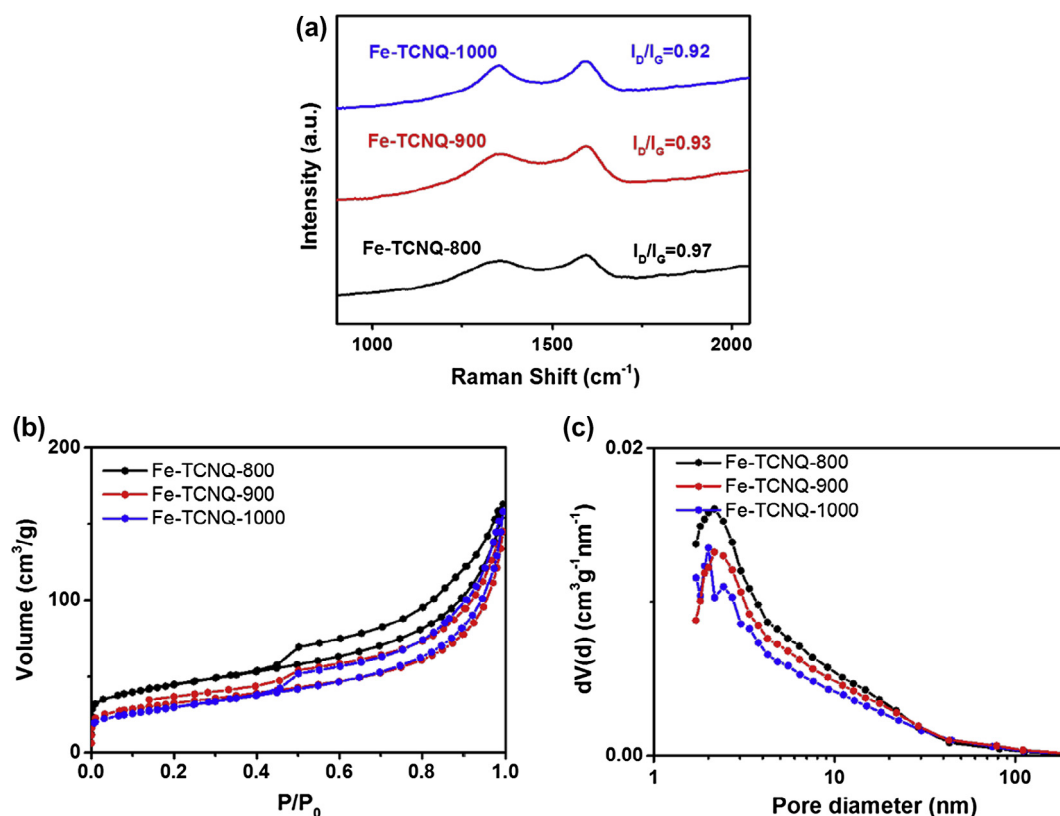

Fig. 4. (a) Raman spectra (b) N$_2$ adsorption–desorption isotherms and (c) the pore size distribution curves of Fe-TCNQ-800, -900, -1000, respectively.
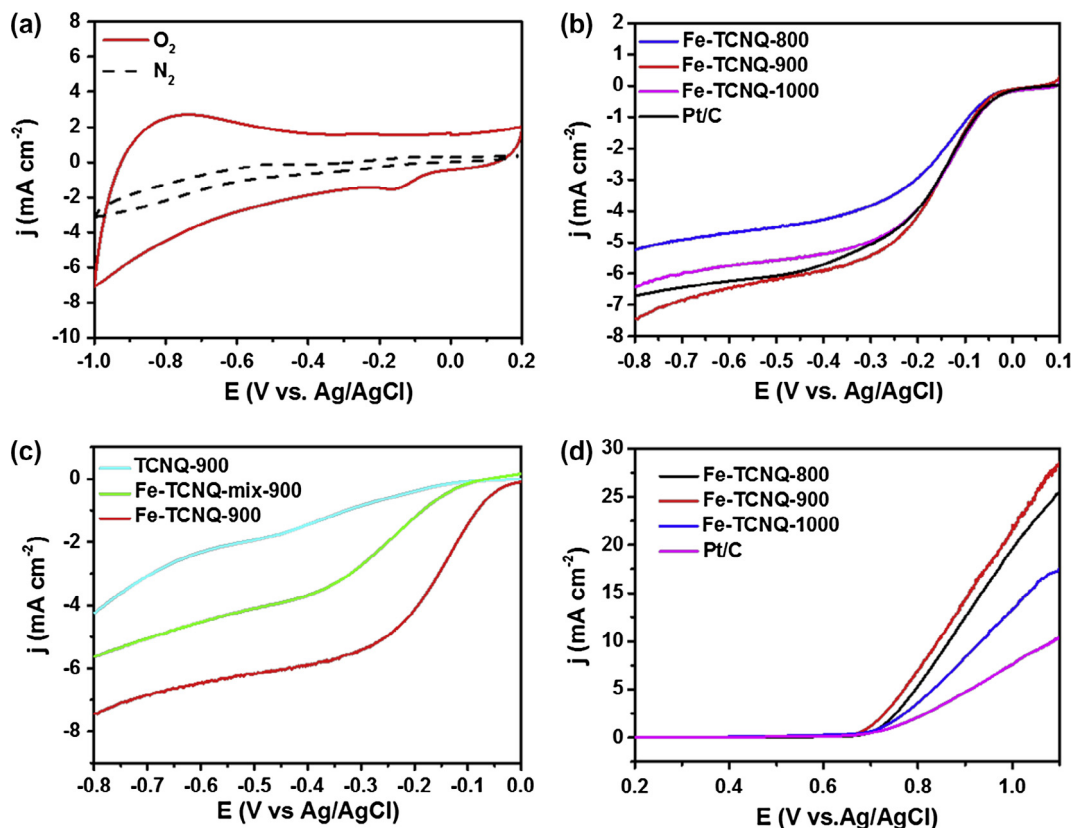
Fig. 5. (a) CV of Fe-TCNQ-900 in N_2 and O_2-saturated 0.1 M KOH; scan rate 50 mV s^{-1}. (b) ORR polarization curves of Fe-TCNQ-800, -900, -1000 and Pt/C. (c) ORR polarization curves of TCN-900, Fe-TCNQ-mix-900, and Fe-TCNQ-900 in an O_2-saturated 0.1 M KOH solution at a rotation speed of 1600 rpm. (d) OER polarization curves of Fe-TCNQ-800, -900, -1000 in N_2-saturated 0.1 M KOH at 1600 rpm.

also showed inferior ORR activity due to the larger Fe$_3$C spheres. So, initially uniform distribution of Fe atoms in MOFs through coordinate bonds seems essential to fabricate more active catalyst, such as avoiding aggregation of Fe$_3$C nanoparticles, in favor of facile charge and mass transfer and uniformly graphitic nitrogen coating [6].

The kinetics of ORR was investigated by LSV from 400 to 2500 rpm and electron transfer number (n) was calculated based on K-L plots. As shown in Figs. S3 and S4, the limiting diffusion current of catalysts was increased at higher rotation speed. Corresponding K-L plots at various potentials exhibited good linearity with a consistent slope, which suggested first-order reaction kinetics. The number of transferred electrons were calculated to be 3.35 (Fe-TCNQ-800), 3.78 (Fe-TCNQ-900), 3.49 (Fe-TCNQ-1000), 3.20 (Fe-TCNQ-mix-900), 2.73 (TCNQ-900), which revealed that a four-electron pathway dominated the ORR process of Fe-TCNQ-900 [39]. More interestingly, the Fe$_3$C@CNx also exhibited a good OER catalytic activity, as shown in the Fig. 5d. The OER activity of catalysts were investigated by using LSV in 0.1 M KOH electrolyte (N$_2$-saturated) with a scan rate of 10 mV s^{-1} and rotation speed at 1600 rpm. The Fe-TCNQ-900 exhibited the highest OER activity among the all the catalysts of different pyrolysis temperature. not only the onset potential of Fe-TCNQ-900 negatively shifted to 0.67 V, the current density at the potential of 1.0 V also increased to 22.07 mA cm^{-2}, which is far superior to the commercial Pt/C catalysts (onset potential is 0.70 V and 7.61 mA cm^{-2} at 1.0 V vs. Ag/AgCl). And the Fe-TCNQ-900 was further compared with ideal noble metal OER catalysts RuO$_2$ in the Fig. S5a. The current density of Fe-TCNQ-900 reached 10 mA cm^{-2} at the potential values of 0.84 V vs. Ag/AgCl, which are close to that (0.75 V vs. Ag/AgCl) of commercial RuO$_2$ catalyst.

The Tafel plots for the ORR and OER on different catalysts were obtained to further investigate the electrode kinetics. The Tafel plots of the as-prepared catalysts were obtained by plotting the logarithm of the kinetic current density from the ORR and OER polarization part in Fig. 5. Fe-TCNQ-900 has the smallest Tafel slope of about 79.93 mV dec^{-1} for ORR and 70.10 mV dec^{-1} for OER among all the as-prepared catalysts, which suggests that Fe-TCNQ-900 undergoes a more favorable kinetics process in alkaline medium (Fig. S5b–d) [40]. Furthermore, the amount of active sites on as prepared catalysts were evaluated by CVs, and electrochemical surface area was estimated from the electrochemical double-layer capacitance (C$_{dll}$) [41]. The C$_{dll}$ value of Fe-TCNQ-900 was calculated to be 3.45 mF m^{-2}, which is higher than these of Fe-TCNQ-800 (2.87 mF m^{-2}) and Fe-TCNQ-1000 (1.39 mF m^{-2}). The largest C$_{dll}$ means that Fe-TCNQ-900 can expose more activate reaction sites. The great ORR and OER catalytic activities of Fe-TCNQ-900 indicated a promising bi-functional electrocatalysts for regenerative fuel cells and rechargeable metal–air batteries.

The stability of Fe-TCNQ-900 for ORR was assessed by chronoamperometric measurements in Fig. 6a. 73% current remained of Fe-TCNQ-900 after 20,000 s continuous tests while Pt/C just maintained 57% of its original current. Additionally, methanol tolerance during ORR is crucial for the potential application in direct methanol fuel cells where methanol may pass across the membrane to deteriorate catalysts. As shown in the Fig. 6b, when 1 M methanol injected into the electrolyte solution at 300 s, Fe-TCNQ-900 exhibited no obvious change in the cathodic current, while Pt/C showed a sharply reduction due to oxidation of methanol, which demonstrated better methanol tolerance of Fe-TCNQ-900.
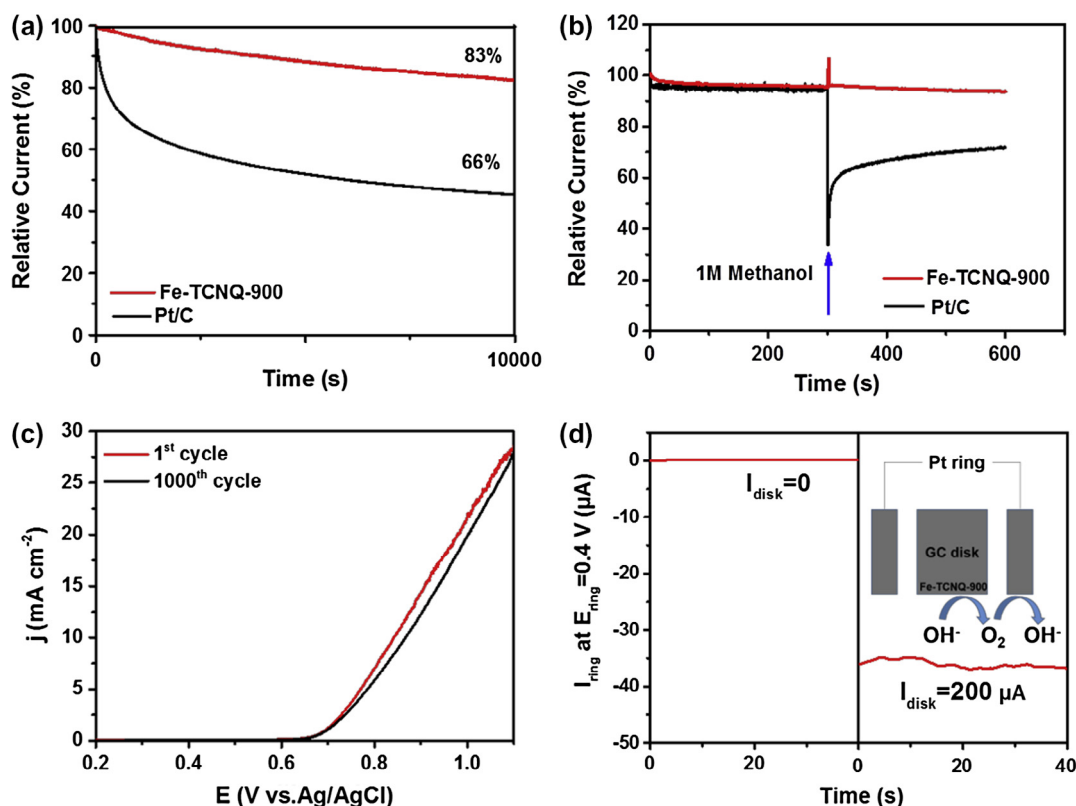
Fig. 6. (a) Chronoamperometric responses of Fe–TCNQ-900 and Pt/C catalysts in O_2-saturated 0.1 M KOH. (b) Chronoamperometric response of Fe–TCNQ-900 and Pt/C catalysts with the addition of methanol. The arrow indicates the addition of methanol. (c) The stability of Fe–TCNQ-900 before and after the 1000 cycles in 0.1 M KOH solution. (d) Ring current of Fe–TCNQ-900 modified RRDE at 1600 rpm in N_2-saturated 0.1 m KOH solution (at 0.40 V). Inset in (d) is a mechanism illustration of the method used to calculate Faradaic efficiency.

Furthermore, the stability of Fe–TCNQ-900 for OER was also displayed in Fig. 6c, after cycling 1000 cycles, the current density of Fe–TCNQ-900 was decreased about 27 mV at 10 mA cm^{-2}, which demonstrated that the Fe–TCNQ-900 structures are stable and practical electrocatalysts for OER. And the Faradaic efficiency was calculated to be 87.5% for the Fe–TCNQ-900 electrode, which denoted a highly selective oxidation of water into O_2. Generally, the difference between E_{ORR} at I = −3 mA cm^{-2} and E_{OER} at I = −10 mA cm^{-2} was employed to assess the overall oxygen electrode catalytic activity, and the smaller difference indicates the potentially practice application. Obviously, the ΔE value of Fe–TCNQ-900 (0.99 V) is less than these of Fe–TCNQ-800 (1.06 V) and Fe–TCNQ-1000 (1.08 V), which is comparable to those of the recently reported electrocatalysts (Table S2).

The progressed ORR and OER electrocatalytic activity of Fe–TCNQ-900 would be due to the following reasons: 1. the Fe–TCNQ precursor guarantee the uniformly distributions of Fe elements, which effectively convert to a core-shell structure with graphitized carbon nitride coating on Fe$_3$C nanoparticles after pyrolysis. 2. The core-shell structure enhance electrocatalytic activities by synergistic effect of strong coupling between Fe$_3$C and nitrogen doped carbon shells. 3. The improved porosity in catalysts through balance bimodal porous can simultaneously facilitate the mass transfer and provide abundant accessible active sites.

4. Conclusion

In conclusion, core-shell structured Fe$_3$C@CNx catalysts have been synthesized through facile and enlargeable process from a readily available MOFs (Fe–TCNQ). Experiment data revealed that the coordinate bonds in MOFs guarantee the uniform distributions

of Fe, which could convert to high active Fe after thermal cracking. Through optimize synthetic procedure, Fe–TCNQ-900 exhibited the best catalytic activity for both ORR and OER, which was superior to commercial Pt/C. Additionally, and showed better resistance to the methanol crossover effect and durability during ORR compare to Pt/C catalyst in 0.10 M KOH solution. The improvement of catalytic activity could attribute to the synergistic effect of strong coupling between Fe$_3$C and nitrogen doped carbon shells, active sites Fe-N$_X$, optimal level of nitrogen doping, and appropriate multimodal porosity. This report provides a new potential way to synthesize core-shell Fe$_3$C@CNx catalysts from MOFs precursors with highly efficient, low cost, facile scale-up able for the commercialization of regenerative fuel cells and rechargeable metal-air batteries.

Appendix A. Supplementary material

Supplementary data associated with this article can be found, in the online version, at https://doi.org/10.1016/j.apsusc.2018.01.056.

References

[1] J.S. Lee, T.K. Sun, R. Cao, N.S. Choi, M. Liu, K.T. Lee, J. Cho, Metal-air batteries with high energy density: Li–air versus Zn–air, Adv. Energy Mater. 1 (2011) 34–50.

[2] G. Nam, J. Park, S.T. Kim, D.-B. Shin, N. Park, Y. Kim, J.-S. Lee, J. Cho, Metal-free Ketjenblack incorporated nitrogen-doped carbon sheets derived from gelatin as oxygen reduction catalysts, Nano Lett. 14 (2014) 1870–1876.

[3] Y. Li, H. Dai, Recent advances in zinc-air batteries, Chem. Soc. Rev. 43 (2014) 5257–5275.

[4] M. Shen, L.-R. Zheng, W. He, C. Ruan, C. Jiang, K. Ai, L. Lu, High-performance oxygen reduction electrocatalysts derived from uniform cobalt–adenine assemblies, Nano Energy 17 (2015) 120–130.

[5] E.M. Erickson, M.S. Thorum, R. Vasić, N.S. Marinković, A.I. Frenkel, A.A. Gewirth, R.G. Nuzzo, In situ electrochemical x-ray absorption spectroscopy of oxygen reduction electrocatalysis with high oxygen flux, J. Am. Chem. Soc. 134 (2012) 197–200.

[6] Z. Li, H. Sun, L. Wei, W.-J. Jiang, M. Wu, J.-S. Hu, Lamellar metal organic framework-derived Fe–N–C non-noble electrocatalysts with bimodal porosity for efficient oxygen reduction, ACS Appl. Mater. Interfaces 9 (2017) 5272–5278.

[7] K. Parvez, S. Yang, Y. Hernandez, A. Winter, A. Turchanin, X. Feng, K. Müllen, Nitrogen-doped graphene and its iron-based composite as efficient electrocatalysts for oxygen reduction reaction, ACS Nano 6 (2012) 9541–9550.

[8] M. Lu, C. Liao, C. Jiang, Y. Du, Z. Zhang, S. Wu, Remarkable high-temperature performance of hollow Co9S8 nanoparticles integrated with carbon materials for lithium-ion batteries, Electrochim. Acta 250 (2017) 196–202.

[9] H. Tang, H. Yin, J. Wang, N. Yang, D. Wang, Z. Tang, Molecular architecture of cobalt porphyrin multilayers on reduced graphene oxide sheets for high-performance oxygen reduction reaction, Angew. Chem. Int. Ed. 52 (2013) 5585–5589.

[10] S.W.T. Price, S.J. Thompson, X. Li, S.F. Gorman, D. Pletcher, A.E. Russell, F.C. Walsh, R.G.A. Wills, The fabrication of a bifunctional oxygen electrode without carbon components for alkaline secondary batteries, J. Power Sources 259 (2014) 43–49.

[11] M. Lefèvre, E. Proietti, F. Jaouen, J.-P. Dodelet, Iron-based catalysts with improved oxygen reduction activity in polymer electrolyte fuel cells, Science 324 (2009) 71–74.

[12] Y. Hu, J.O. Jensen, W. Zhang, L.N. Cleemann, W. Xing, N.J. Bjerrum, Q. Li, Hollow spheres of iron carbide nanoparticles encased in graphitic layers as oxygen reduction catalysts, Angew. Chem. Int. Ed. 53 (2014) 3675–3679.

[13] D. Deng, L. Yu, X. Chen, G. Wang, L. Jin, X. Pan, J. Deng, G. Sun, X. Bao, Iron encapsulated within pod-like carbon nanotubes for oxygen reduction reaction, Angew. Chem. Int. Ed. 52 (2013) 371–375.

[14] J. Li, M. Zou, L. Chen, Z. Huang, L. Guan, An efficient bifunctional catalyst of Fe/Fe3C carbon nanofibers for rechargeable Li-O2 batteries, J. Mater. Chem. A 2 (2014) 10634–10638.

[15] J. Yang, J. Hu, M. Weng, R. Tan, L. Tian, J. Yang, J. Amine, J. Zheng, H. Chen, F. Pan, Fe-cluster pushing electrons to N-doped graphitic layers with Fe3C(Fe) hybrid nanostructure to enhance O2 reduction catalysis of Zn-air batteries, ACS Appl. Mater. Interfaces 9 (2017) 4587–4596.

[16] B.Y. Guan, L. Yu, X.W. Lou, A dual-metal-organic-framework derived electrocatalyst for oxygen reduction, Energy Environ. Sci. 9 (2016) 3092–3096.

[17] J.-S. Li, S.-L. Li, Y.-J. Tang, M. Han, Z.-H. Dai, J.-C. Bao, Y.-Q. Lan, Nitrogen-doped Fe/Fe3C@graphitic layer/carbon nanotube hybrids derived from MOFs: efficient bifunctional electrocatalysts for ORR and OER, Chem. Commun. 51 (2015) 2710–2713.

[18] S. Sun, P. Wu, D. Zhu, The preparation, characterization of amorphous Cu–TCNQ film with a low degree of charge-transfer (DCT) and its electric switching properties, Thin Solid Films 301 (1997) 192–196.

[19] D.F. Shriver, S.A. Shriver, S.E. Anderson, Ligand field strength of the nitrogen end of cyanide and structures of cubic cyanide polymers, Inorg. Chem. 35 (1988) 322–323.

[20] J. Jo, M.-J. Jin, J. Park, V. Modepalli, C.-Y. Kao, A.J. Epstein, M. Choi, N. Park, S.-Y. Lee, C. Jeon, J.-W. Yoo, Organic-based magnetic semiconductor thin film of Fe (TCNQ)x~2 developed by physical vapor deposition and local spin density induced core-level shifts, Synth. Met. 196 (2014) 56–60.

[21] H. Wang, T. Maiyalagan, X. Wang, Review on recent progress in nitrogen-doped graphene: synthesis characterization, and its potential applications, ACS Catal. 2 (2012) 781–794.

[22] Z.-H. Sheng, L. Shao, J.-J. Chen, W.-J. Bao, F.-B. Wang, X.-H. Xia, Catalyst-free synthesis of nitrogen-doped graphene via thermal annealing graphite oxide with melamine and its excellent electrocatalysis, ACS Nano 5 (2011) 4350–4358.

[23] D. Geng, Y. Chen, Y. Chen, Y. Li, R. Li, X. Sun, S. Ye, S. Knights, High oxygen-reduction activity and durability of nitrogen-doped graphene, Energy Environ. Sci. 4 (2011) 760–764.

[24] Q. Li, S. Zhang, L. Dai, L.-S. Li, Nitrogen-doped colloidal graphene quantum dots and their size-dependent electrocatalytic activity for the oxygen reduction reaction, J. Am. Chem. Soc. 134 (2012) 18932–18935.

[25] P. Chen, L. Wang, G. Wang, M. Gao, J. Ge, W. Yuan, Y. Shen, A. Xie, S. Yu, Nitrogen-doped nanoporous carbon nanosheets derived from plant biomass: an efficient catalyst for oxygen reduction reaction, Energy Environ. Sci. 7 (2014) 4095–4103.

[26] L. Lin, Q. Zhu, A.-W. Xu, Noble-metal-free Fe–N/C catalyst for highly efficient oxygen reduction reaction under both alkaline and acidic conditions, J. Am. Chem. Soc. 136 (2014) 11027–11033.

[27] R. Liu, D. Wu, X. Feng, K. Müllen, Nitrogen-doped ordered mesoporous graphitic arrays with high electrocatalytic activity for oxygen reduction, Angew. Chem. Int. Ed. 49 (2010) 2565–2569.

[28] D. Chen, G. Ji, Y. Ma, J.Y. Lee, J. Lu, Graphene-encapsulated hollow Fe3O4 nanoparticle aggregates as a high-performance anode material for lithium ion batteries, ACS Appl. Mater. Interfaces 3 (2011) 3078–3083.

[29] L. Lai, J.R. Potts, D. Zhan, L. Wang, C.K. Poh, C. Tang, H. Gong, Z. Shen, J. Lin, R.S. Ruoff, Exploration of the active center structure of nitrogen-doped graphene-based catalysts for oxygen reduction reaction, Energy Environ. Sci. 5 (2012) 7936–7942.

[30] R.A. Sidik, A.B. Anderson, N.P. Subramanian, S.P. Kumaraguru, B.N. Popov, O2 reduction on graphite and nitrogen-doped graphite: experiment and theory, J. Phys. Chem. B 110 (2006) 1787–1793.

[31] H. Kim, K. Lee, S.I. Woo, Y. Jung, On the mechanism of enhanced oxygen reduction reaction in nitrogen-doped graphene nanoribbons, Phys. Chem. Chem. Phys. 13 (2011) 17505–17510.

[32] W.-J. Jiang, L. Gu, L. Li, Y. Zhang, X. Zhang, L.-J. Zhang, J.-Q. Wang, J.-S. Hu, Z. Wei, L.-J. Wan, Understanding the high activity of Fe–N–C electrocatalysts in oxygen reduction: Fe/Fe3C nanoparticles boost the activity of Fe–Nx, J. Am. Chem. Soc. 138 (2016) 3570–3578.

[33] R. Cao, R. Thapa, H. Kim, X. Xu, K.M. Gyu, Q. Li, N. Park, M. Liu, J. Cho, Promotion of oxygen reduction by a bio-inspired tethered iron phthalocyanine carbon nanotube-based catalyst, Nat. Commun. 4 (2013) 2076–2209.

[34] L. Qu, Y. Liu, J.-B. Baek, L. Dai, Nitrogen-doped graphene as efficient metal-free electrocatalyst for oxygen reduction in fuel cells, ACS Nano 4 (2010) 1321–1326.

[35] Z. Li, Y. Wang, H. Sun, W. Wu, M. Liu, J. Zhou, G. Wu, M. Wu, Synthesis of nanocomposites with carbon-SnO2 dual-shells on TiO2 nanotubes and their application in lithium ion batteries, J. Mater. Chem. A 3 (2015) 16057–16063.

[36] Y. Mao, H. Duan, B. Xu, L. Zhang, Y. Hu, C. Zhao, Z. Wang, L. Chen, Y. Yang, Lithium storage in nitrogen-rich mesoporous carbon materials, Energy Environ. Sci. 5 (2012) 7950–7955.

[37] G. Wu, C.M. Johnston, N.H. Mack, K. Artyushkova, M. Ferrandon, M. Nelson, J.S. Lezamapacheco, S.D. Conradson, K.L. More, D.J. Myers, Synthesis–structure–performance correlation for polyaniline–Me–C non-precious metal cathode catalysts for oxygen reduction in fuel cells, J. Mater. Chem. 21 (2011) 11392–11405.

[38] J. Zheng, L. Tian, Y. Duan, L. Lin, S. Cui, H. Peng, T. Liu, H. Guo, X. Wang, F. Pan, A core–shell nanohollow-γ-Fe O @graphene hybrid prepared through the Kirkendall process as a high performance anode material for lithium ion batteries, Chem. Commun. 51 (2015) 7855–7858.

[39] Z.-Y. Wu, X.-X. Xu, B.-C. Hu, H.-W. Liang, Y. Lin, L.-F. Chen, S.-H. Yu, Iron carbide nanoparticles encapsulated in mesoporous Fe-N-doped carbon nanofibers for efficient electrocatalysis, Angew. Chem. Int. Ed. 54 (2015) 8179–8183.

[40] Z. Wang, M. Li, L. Fan, J. Han, Y. Xiong, Fe/Ni-N-CNFs electrochemical catalyst for oxygen reduction reaction/oxygen evolution reaction in alkaline media, Appl. Surf. Sci. 401 (2017) 89–99.

[41] W. Li, S. Zhang, Q. Fan, F. Zhang, S. Xu, Hierarchically scaffolded CoP/CoP2 nanoparticles: controllable synthesis and their application as a well-matched bifunctional electrocatalyst for overall water splitting, Nanoscale 9 (2017) 5677–5685.